Direct numerical simulations of multifluid flows in a vertical channel undergoing topology changes

Jiacai Lu* and Gretar Tryggvason
Department of Mechanical Engineering, Johns Hopkins University, Baltimore, Maryland, USA

(Received 26 September 2017; published 30 August 2018)

Multifluid flows in a vertical channel are examined by direct numerical simulations, for situations where the topology of the interface separating the different fluids changes. Several bubbles are initially placed in a turbulent channel flow at a sufficiently high void fraction so that the bubbles collide and the liquid film between them becomes very thin. This film is ruptured at a predetermined thickness and the bubbles are allowed to coalesce. For the cases with high surface tension the bubbles continue to coalesce, eventually forming one large bubble. At low surface tension, on the other hand, the large bubbles break up again, sometimes undergoing repeated coalescence and breakup. The evolution of various integral quantities, such as the average flow rate, wall shear, and interface area, are monitored and compared for different governing parameters. Averages of the flow field and the phase distribution over planes parallel to the walls are also examined, and the microstructure, at statistically steady state, is examined using low-order probability functions.

DOI: 10.1103/PhysRevFluids.3.084401

I. INTRODUCTION

Direct numerical simulations (DNS) have been used to examine several bubbly multiphase flows, leading to considerable new insights. Such simulations include both studies of single bubbles, such as Refs. [1–5], which examined how the shape and path of a buoyant bubbles depends on the governing parameters, two bubbles [6], as well as the interactions of many freely evolving bubbles, both in fully periodic domains [7,8] and in channels [9–13]. These simulations have clarified the effect of deformability and void fraction on the collective behavior of bubbles. They have shown, for example, that while nearly spherical bubbles tend to line up side by side, deformable bubbles are more likely to follow each other, and that spherical bubbles experience much stronger lift than more deformed ones. The dependency of lift on deformability results in major changes in the void fraction distribution in channels as the bubble size increases. Bubbly flows are, however, only one of several possible flow regimes, and even when it is possible to identify distinct bubbles, in high void fraction flows we expect them to frequently coalesce and break apart. In many cases the gas and the liquid are so intermingled that identifying bubbles (or drops) is impossible. The structure of such flows depends sensitively on the governing parameters, and, in particular, the configuration of the phase boundary is found to undergo very significant changes as the flow parameters are changed. At low void fraction the gas typically is found as distinct bubbles dispersed in the flow, but as the void fraction is increased the bubbles coalesce and break up in a chaotic manner in a regime often referred to as churn-turbulent flow. At even higher void fraction the bubbles coalesce into slugs, and eventually the liquid flows along the walls, in annular flows. In addition to the average void fraction, the fluid velocity modifies each flow regime and when they transition from one to the other. High void fraction flows, where

*Corresponding author: jiacai.lu@jhu.edu

the interface between the different fluids constantly undergoes topology changes, are obviously of significant importance for many applications, and here we examine such flows using DNS.

Although many DNS studies of bubbly flows have been carried out, simulations of more complex multiphase pipe or channel flows are not as common. A few DNS studies of annular flows include Refs. [14,15], but simulations of flows undergoing extensive topology changes have mostly focused on atomization, including at high Weber numbers where liquid jets form drops much smaller than their diameter. Examples of such studies can be found in Refs. [16–18]. Although simulations of atomization have already yielded major new insights into how liquid jets break up into droplets, they have also showed the difficulties in obtaining reliable results for multiphase flows undergoing massive topology change. In almost all cases, very small-scale features that often form spontaneously during coalescence and breakup are not fully resolved, and in most cases the small-scale physics ultimately responsible for topology change is not included. This often leads to grid-dependent topology changes, particularly for methods that advect a marker function identifying the different fluids directly on a fixed grid. Here we used connected marker particles to follow the interface, thus giving us more control over the topology change. However, although we avoid automatic grid-dependent topology changes, we do not solve the full problem. Instead we impose grid independent, but artificial, conditions to determine when coalescence takes place. We examine the influence of changing these conditions on the overall solution and attempt to quantify the effect.

Many authors have conducted experimental studies of multiphase flow in vertical pipes. For adiabatic flows those include Refs. [19–22]. Recent experiments include Ref. [23], which examined the effect of surfactants, and studies of flashing flows by Ref. [24]. Since the flow characteristics change in fundamental ways during a transition from one regime to another, many authors have attempted to construct maps that show the boundary between the different regimes as functions of the governing parameters. Early proposals can be found in Refs. [25,26]. A brief overview of the different maps that have been proposed is given by Ref. [27]. For a review of experiments and modeling of air liquid flows in vertical pipes, with a focus on gas-lift pumps for oil recovery, see Ref. [28], for example. Modeling such flows is still very primitive, and we expect DNS to be able to cast considerable light on the various processes governing the flow.

II. NUMERICAL METHOD

The flow in the whole computational domain is described by the "one-fluid" Navier-Stokes equations

$$\rho\frac{\partial \mathbf{u}}{\partial t} + \rho\nabla\mathbf{u}\mathbf{u} = -\nabla p + \rho\mathbf{g} + \nabla\cdot\mu(\nabla\mathbf{u} + \nabla\mathbf{u}^T) + \sigma\int_F \kappa_f \mathbf{n}_f \delta(\mathbf{x}-\mathbf{x}_f)\,dA_f. \tag{1}$$

Here $\mathbf{u}$ is the velocity vector, ρ and μ are the discontinuous density and viscosity fields, respectively, and $\mathbf{g}$ is the gravity acceleration. The last term on the right-hand side represents the surface tension as a concentrated force on the front or interface. The surface tension σ is constant and δ is a three-dimensional delta function constructed by repeated multiplication of one-dimensional delta functions. κ_f is twice the mean curvature, $\mathbf{n}_f$ is a unit vector normal to the front, $\mathbf{x}$ is the point at which the equation is evaluated, and $\mathbf{x}_f$ is the position of the front. The momentum equations are supplemented by the incompressibility conditions $\nabla\cdot\mathbf{u} = 0$, which leads to a nonseparable elliptic equation for the pressure.

The equations are solved on a regular structured staggered grid, using a front-tracking/finite-volume method. Time integration is done by a second-order predictor-corrector method, the viscous terms are discretized by second-order centered differences, and the advection terms are approximated using a QUICK scheme. The pressure equation is solved using the semicoarsening multigrid method PFMG/SMG from the HYPRE library [29] to impose a divergence-free velocity field. To advect the density and the viscosity fields, and to accurately compute the surface tension, the fluid interface is tracked by connected marker points (referred to as the "front"). The front points are connected to form an unstructured surface grid that is advected by the fluid velocity, interpolated from the fixed grid.

The front usually deforms, and surface markers are dynamically added and deleted as needed. If a side of a triangular interface element becomes longer than half the grid spacing of the fixed fluid grid the side is split, creating two new triangular elements and if a side is shorter then one fourth of the grid spacing, the side is collapsed to a point, removing two surface elements. For a detailed discussion see Ref. [30]. The surface tension is represented by a distribution of singularities (delta functions) located at the front. The gradients of the density and viscosity become delta functions when the change is abrupt across the boundary and are transferred to the fixed grid by approximating them by smoother functions, with a compact support. At each time step, after the front has been advected, the density and the viscosity fields are reconstructed by integration of the smooth grid-delta function. Here we use the function originally introduced by Peskin [31], which results in an artificial interface thickness of about three grid spaces. As long as this thickness is smaller than other length scales, such as radius of curvature, the interface evolution is not affected; see Ref. [30]. The surface tension is then added to the nodal values of the discrete Navier-Stokes equations. The method was introduced by Ref. [32], and for a description of the original method, as well as various improvements and refinements, see Refs. [30,33]. The method has been applied to several multifluid problems and tested and validated in a number of ways. Those tests include comparisons with analytical solutions for simple problems, other numerical computations, and experiments. The actual resolution requirement varies with the governing parameters of the problem. High Reynolds number flows, for example, generally require finer resolution than low Reynolds number flows, as in other numerical calculations. For applications to bubbly flows, see Refs. [7,8,34,35], for example. For other implementation of similar ideas and applications to bubbly flows, see Refs. [1–3,36–38], for example.

Topology changes in multiphase flows take place through two primary mechanisms: films that rupture and threads that break. DNS must be able to accurately handle both. For methods that track the indicator function identifying the different fluids or phases directly on an Eularian grid (such as VOF or level set methods), topology change will take place when the resolution of a film or a thread is sufficiently low, whereas methods that use connected marker points to track the interface will generally not allow a change in topology. Both methods can be modified to either allow or prevent topology changes, but at the cost of additional code and possibly increased runtime. Of the two types of topology changes, thin threads that break are by far the easier to deal with. The Navier-Stokes equations predict that the diameter of threads can become zero in a finite time, and no additional physical modeling needs to be included. Furthermore, the breakup is fast, so while there may be a moment just before the thread breaks when it is not well resolved, this is often such a short time that it does not have a significant effect on the overall dynamics of the flow. Both types of methods generally handle thread breakup easily, with marker point methods leaving an inert string of particles behind. The rupture of thin films is a much more complex matter. The thickness of a draining film, simulated using the standard Navier-Stokes equations, does not usually become zero in a finite time, and it is only because of the presence of short-range attractive forces (usually not included) that it eventually becomes unstable and holes are formed. The initial hole is then enlarged by either the formation of other holes that merge with the first one or the enlargement of the original hole by rim retreat and breakup. The breakup includes the formation of drops with threads that snap, but often on such a small scale that it is difficult to resolve them fully in simulations focusing on a larger region of the flow. The rupture of films in simulations using numerical methods that track the indicator function directly is an artifact of the finite resolution, and in some cases it is found that refining the grid postpones the rupture and prevents the solution from converging to a grid-independent form. While in many cases such methods produce results that look “physical,” it is not well understood when the rupture is adequately controlled artificially by the resolution and when more complete rupture models must be included. When the interface is tracked by connected marker points it is necessary to add a strategy to rupture the interfaces when they are close enough, and this results in a complete control of when, or under what circumstances, rupture takes place, thus allowing us to examine how sensitive the overall evolution of the flow is to how the rupture takes place, even if a complete rupture model is not included.

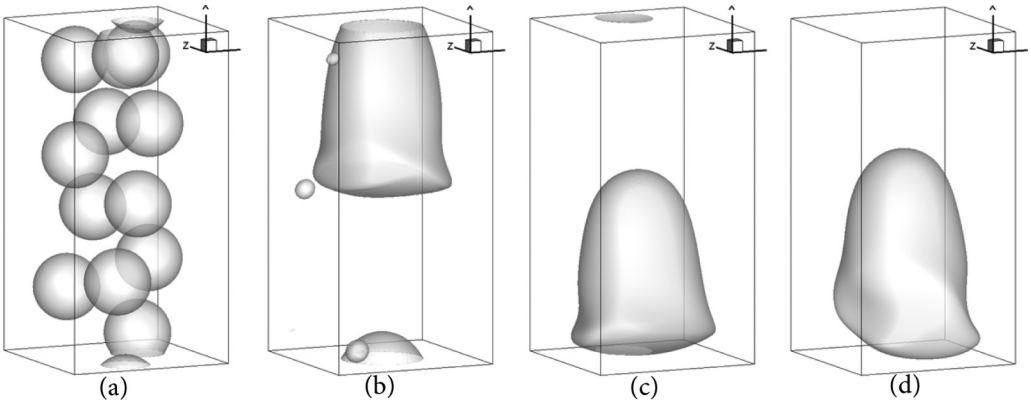

FIG. 1. The effect of the resolution on the coalescence of several bubbles into a large one. The initial bubble distribution is shown in panel (a), and the results as computed at time 40 on $128 \times 64 \times 64$, $192 \times 96 \times 96$, and $256 \times 128 \times 128$ grids are shown in panels (b)–(d), respectively.

In the present simulations the topology change is accomplished by reconnecting fronts that are closer than a prescribed minimum distance. The topology change algorithm consists of two steps: the identification of close front points and the actual restructuring. To identify close points, we divide the domain into subdomains and construct a linked list of points in each domain so that we can limit the search to points in each subdomain. Once close points have been identified, we merge all close points and finally eliminate links between merged points. Unconnected points are then deleted. In the actual topology change code, we have implemented a number of steps to increase its efficiency, but none of these steps affect the eventual outcome.

We emphasize that the coalescence criteria can be specified independently from the grid resolution. However, even if we keep the coalescence criteria constant, the grid resolution can influence how thin a film can become and therefore change the results. This is discussed in the next section.

III. RESOLUTION TEST AND THE EFFECT OF THE CRITICAL COALESCENCE DISTANCE

Before examining the evolution of more complex flows, we first investigate simpler problems to establish the resolution needed and how coalescence should be treated. For these tests we use a vertical laminar channel which is bounded by two parallel rigid walls in the y direction. The flow is driven by an applied pressure gradient dP/dx in the x direction. Both the streamwise (x) and spanwise (z) directions are periodic. The computational domain size in computational units is $2 \times 1 \times 1$ in the x, y, and z directions, respectively. Initially, the Reynolds number based on the maximum streamwise velocity and the channel width is 1000, and 12 bubbles of diameter $d = 0.4$ are randomly placed into the flow, giving a void fraction of 20.1%. The Eötvös number (Eo $\equiv \rho_f g d^2/\sigma$) is 0.8, and the Morton number [Mo $\equiv g\mu^4/(\rho\sigma^3)$] is 2.0×10^{-7}, where ρ and μ are the density and viscosity of the heavy fluid, and g, d, and σ are the gravitational acceleration in the negative x direction, the initial bubble diameter, and the surface tension coefficient, respectively. The density and viscosity ratios between the heavy fluid and light bubbles are 20. To assess the resolution needed to obtain a converged solution, we ran three cases where the critical distance for coalescence was held constant but the grid resolution varied. Figure 1(a) shows the initial bubble distribution for all cases, and Figs. 1(b)–1(d) show the results at time 40 for a $128 \times 64 \times 64$ grid, a $192 \times 96 \times 96$ grid, and a $256 \times 128 \times 128$ grid, respectively. The 12 initial bubbles have coalesced into one large bubble at this time, and the results for the finest two grids are very close, while the results on the coarser grid are significantly different. The difference in surface area of the bubbles on the finest grids at time 40 is, for example, only 1.16%. The results are also compared in Fig. 2, where the time evolution of the average wall shear is shown in the top frame and the projection of the surface area onto the

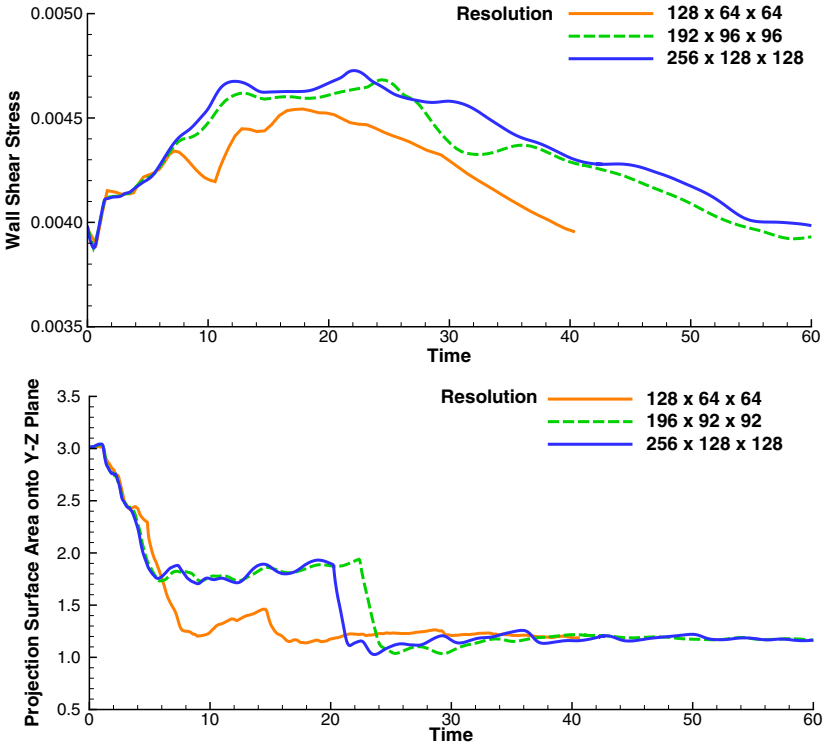

FIG. 2. The effect of the resolution on the average wall shear (top) and the surface area projected onto a plane perpendicular to the flow direction (bottom).

y-z plane in the bottom frame. Again, it is clear that the two finer grids give similar results, although the projected area shows a slight delay in the final coalescence for the medium grid compared to the finest one. The low resolution is, on the other hand, significantly different. We have quantified the differences by computing root mean square of the difference for the whole time interval and found that the difference in the wall shear stress is 1.5% between the two finest resolutions. The difference in the projected surface area, computed in the same way, is, however, larger (10%) since the bubbles coalesce into one large bubble at different times.

To assess the effect of the critical coalescence distance, δ, on the results, in Fig. 3 we keep the resolution constant (equal to $192 \times 96 \times 96$ grid points) but vary the critical coalescence distance. The initial bubble distribution for all cases is shown in Fig. 3(a), and the bubbles are shown at time 40 in Figs. 3(b)–3(d), with δ equal to 0.006, 0.003, and 0.0015, respectively. The results for the first two δ values are fairly similar (although the shapes of two bubbles are a little different, their surface area difference is less than 0.1%), but the result in Fig. 3(d), for the smallest δ, is different. The differences are also clear in Fig. 4, where we plot the wall shear stress in the top frame and the projection of the surface area onto the y-z plane in the bottom frame versus time, for the values of δ shown in these two frames as well as one smaller and one larger value (0.00075 and 0.012). Although there are slight differences between the results for the three largest δ values, they are fairly similar and very different from what is seen for the lowest two values. Specifically, the average root mean square difference in wall shear stress over the whole time simulated, between the case with a critical coalescence distance of 6.0×10^{-3} and the one with a distance of 3.0×10^{-3}, is 2.15%. These results are obtained using uniform grid resolution where the grid spacing is $h = 0.0102$, so the ratio of the critical coalescence distance over the grid spacing is $\delta/h = 1.176$, 0.588, 0.294, 0.147, and 0.0735, respectively, suggesting that the results are insensitive to the exact value of δ, for δ equal

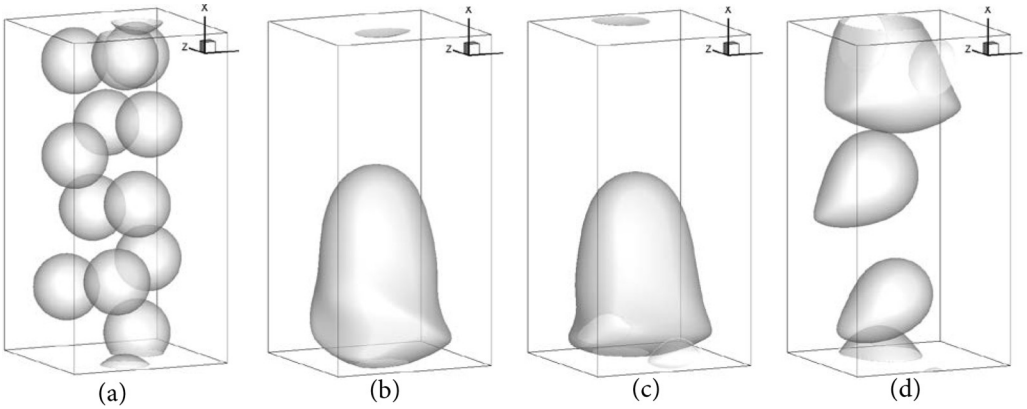

FIG. 3. The effect of the critical coalescence distance on the coalescence of several bubbles. The initial bubble distribution is shown in panel (a), and the results at time 40 for the critical distance of 0.006, 0.003, and 0.0015 are shown in panels (b)–(d), respectively.

to about a quarter to one grid spacing. The critical coalescence distance for the runs in Figs. 1 and 2 was taken to be $\delta = 0.003$, so the ratio δ/h is equal to 0.192, 0.294, and 0.384. Thus, the two finer grids are also within the range where the results appear to be relatively insensitive to the critical distance for coalescence.

We have also examined one case where we change the resolution but keep the ratio of delta over grid spacing constant, $\delta/h = 0.384$. Using the same grid as for the resolution study we found that the evolution was similar, although not exactly identical. The tests presented here suggest that it is possible to get fairly consistent results for flows undergoing repeated bubble coalescence, where the overall behavior is relatively insensitive to the exact coalescence criteria and the grid resolution. The coalescence criteria and the resolution must be selected to be consistent and of roughly the same order of magnitude, but the exact value does not seem to be critical. Further investigation of the sensitivity is ongoing.

IV. EFFECT OF SURFACE TENSION

One of the advantages of computational studies is that it is easy to change just one aspect of the problem, in isolation. Here we focus on the effect of bubble deformability. We use a similar computational domain as for the tests in the last section, but with different size of $\pi \times 0.5\pi \times 2$ in the streamwise (x), spanwise (z), and the wall-normal (y) direction. The flow is also driven upward by an imposed pressure gradient, but the initial velocity field is a steady-state turbulent flow with a friction Reynolds number of 128. Initially, 40 bubbles are placed randomly in the channel. The diameter of each bubble is 0.4, giving a void fraction of 13.58%. The density of the heavy fluid is 1.0, and the density of the light fluid is 0.1. The heavy and the light fluid viscosities are both taken to be 3.333×10^{-4} and the gravitational acceleration is 0.1, acting in the negative x direction. The initial turbulent flow is generated using a spectral code [39,40], and the bubbles are simply placed in the flow, requiring the flow to adjust to the bubbles in the first few time steps. For the high surface tension cases a laminar initial flow will lead to a similar evolution as the turbulent flow field used here, but for the lower surface tension cases an initially laminar flow will result in the initial bubbles simply stretching into long filaments parallel to the flow. Using an initially turbulent flow prevents this and ensures that the bubbles collide with each other. The objective of the present investigation is to document the effect of surface tension, or bubble deformability, on the evolution, and to do so we conduct a series of simulations where all parameters have been kept constant except for the surface tension. The surface tension coefficient σ, the corresponding Eötvös number Eo based on the initial bubble diameter, and the Morton number Mo are listed in Table I. For the simulations presented

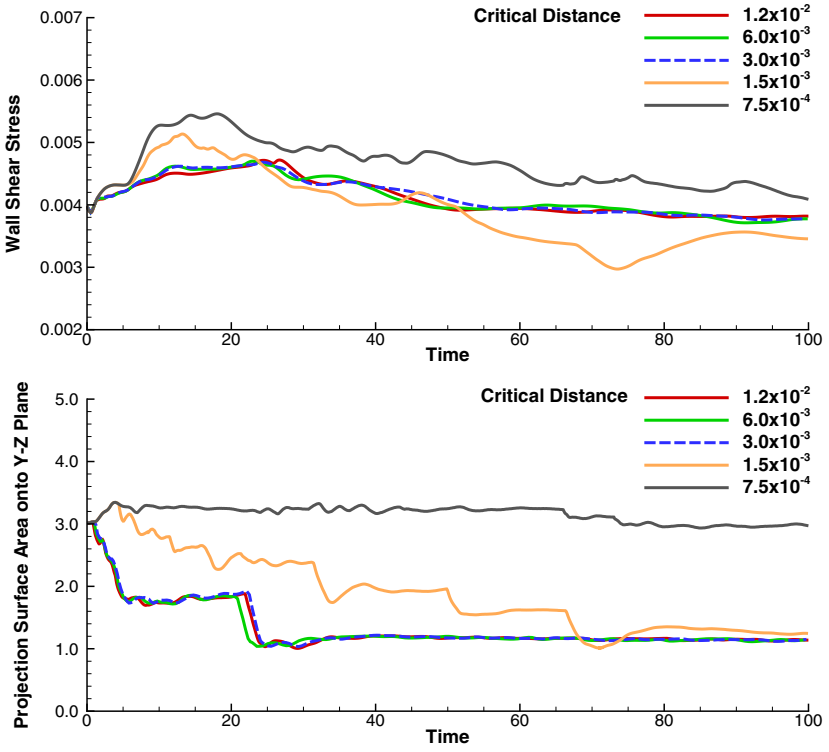

FIG. 4. The effect of the critical coalescence distance on the average wall shear (top) and the surface area projected onto a plane perpendicular to the flow direction (bottom). Results for five different coalescence criteria are shown.

in this section we use a grid that is 192 (uniform) × 96 (uniform) × 128 (nonuniform) cells. The smallest and biggest cell sizes in the wall-normal direction are 0.003549 and 0.023 in computational units. We note that we present all results in computational, rather than nondimensional, units to reduce the probability of error or misinterpretation.

The interface separating the light and the heavy fluid is shown in Fig. 5 for five different times for the four cases. The times have been selected to give an impression of how the flow evolves and are not evenly spaced in time. In cases 1 and 2 the surface tension is sufficiently high so that the bubbles continuously merge to form larger and larger bubbles, until most of the light fluid is contained in one large bubble. While the final bubble in case 1 is ellipsoidal, the final bubble in case 2 is more like a "bullet"-shaped Taylor bubble. There are smaller bubbles present in case 2, formed during the formation of the large bubble, but those will eventually merge with it. The evolution for the lower surface tension is very different. In both cases 3 and 4 the bubbles initially merge into larger bubbles, but these are deformed significantly by the flow, and as they grow larger through continuing coalescence they also start to break up. At the latest time we see a few large bubbles and many

TABLE I. Parameters list for all cases for effect of surface tension.

	Case 1	Case 2	Case 3	Case 4
Surface tension (σ)	0.08	0.01	0.004	0.002
Eötvös number (Eo)	0.2	1.6	4.0	8.0
Morton number (Mo)	2.41×10^{-12}	1.23×10^{-9}	1.93×10^{-8}	1.54×10^{-7}

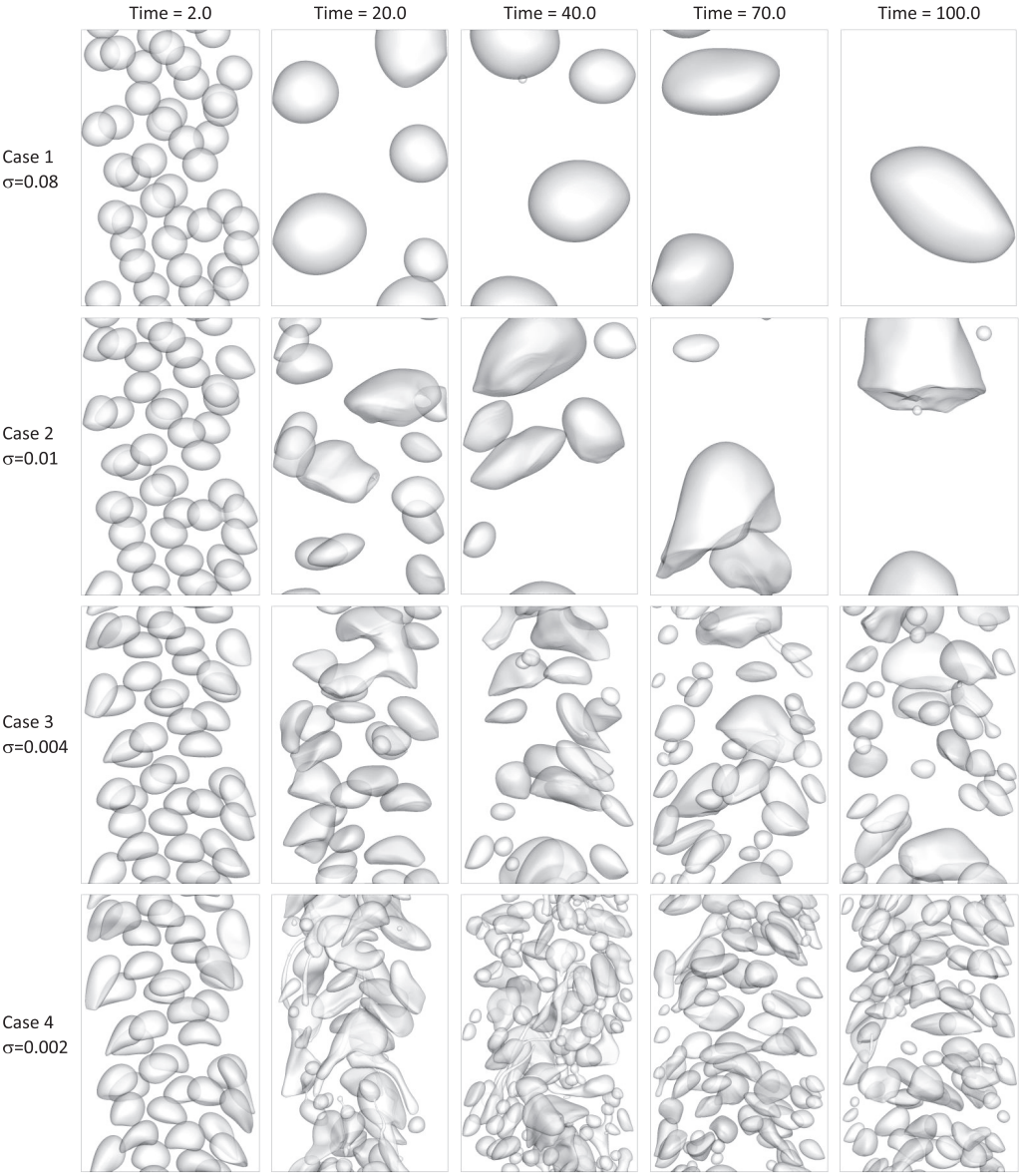

FIG. 5. The fluid interface at five times for four cases with different surface tension. The rows represent different cases, and columns show different times of 2.0, 20.0, 40.0, 70.0, and 100.0.

smaller bubbles for both cases, but the distribution of bubble sizes is different. In the last frame of case 3 the large bubbles are significantly larger than the bubbles at the initial time and the smaller bubbles much smaller, while in case 4 the final larger bubbles are smaller and we see more small bubbles. The intermediate stages are also very different with significantly more complex evolution taking place for the smallest surface tension, including the formation of long filaments of the light fluid.

In addition to the interface, we have also examined the structure of the vorticity field. In Fig. 6 we visualize the vorticity at a late time of 90, after the bubbles have coalesced and broken up, for the lower surface tension cases, for all four cases. The vortices are visualized using the λ_2 method,

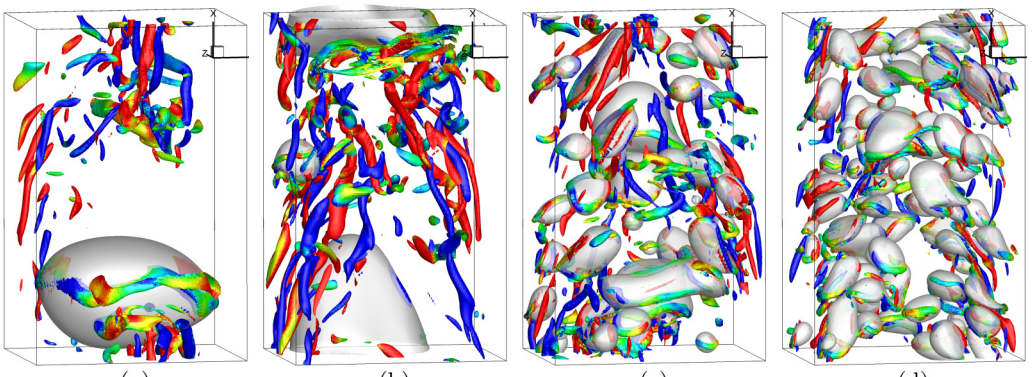

FIG. 6. The bubbles and the vortical structures at a late time for all four cases. The isosurfaces of vortices represent $\lambda_2 = -5.0$. (a) case 1; (b) case 2; (c) case 3; (d) case 4.

and the color shows their orientation. Red and blue indicate vortices aligned with the flow, but with rotation of the opposite sign, and the green and yellow vortices are perpendicular to the flow. The λ_2 value shown here for all cases is -5.0. While the initial velocity field is turbulent, the bubble motion quickly changes the structure of the turbulence in major ways. For case 1 the vorticity is mostly confined to the wake of the bubble, and for case 2 this seems to be also true, although the vorticity is now shed from the rim of the bubble. For cases 3 and 4 most of the vorticity also seems to be generated by the bubbles.

The averaged void fraction versus the wall-normal coordinate is shown for four times in Fig. 7 (left column) for all four runs. As the bubbles are evenly distributed in the channel at initial time, its corresponding distribution of averaged void fraction is flat for all cases. It is clear that the void fraction fluctuates significantly more for the first two cases than for the last two. Indeed, for the last case with the lowest surface tension the void fraction remains more or less unchanged, except for the early time. For the highest surface tension the final profile corresponds to a single bubble moving in the center of the channel. The average liquid velocity, plotted in the right column of Fig. 7, shows similar evolution. For the lower surface tension cases (bottom two rows) it is more or less unchanged, but for the highest surface tension case (top row) the flow rate is reduced and the final time shows a profile peaked in the center of the channel.

The evolution of various quantities averaged over the whole channel is shown in Fig. 8. The top panels show the volumetric flow of the heavy and the light fluid, and it is clear that the heavy fluid flow rate decreases most for the largest surface tension, but stays essentially constant for the lowest value. The bubbles are initially injected with the velocity of the heavy fluid so they first accelerate rapidly due to buoyancy and then their velocity fluctuates significantly more than the liquid velocity. Nevertheless, the light fluid velocity is comparable for all cases, except for the highest surface tension, where the velocity decreases once the bubbles are large enough. The average wall shear stress is shown in Fig. 8(c). At time zero, the pressure gradient driving the flow and the weight of the mixture balance the wall shear. As the bubbles are released, the nearly spherical bubbles in the high surface tension cases initially move to the wall due to lift forces and increase the wall shear stress. Their accumulation at the wall does, however, lead to rapid coalescence. The more deformable bubbles (the lower surface tension cases) have smaller lift force and do not move to the wall and the wall shear varies less. As the bubbles in the high surface tension case coalesce they move to the center of the channel, and since the bubble becomes ellipsoidal, it tends to block the channel and thus slow down the flow. Lower surface tension leads to more deformed bubbles, so even when they are large, they block the flow less and thus lead to smaller reduction in flow rate. Once the flow reaches an approximately steady state, the average wall shear stresses for all cases are roughly equal to their initial value, where the average wall shear balances the imposed pressure gradient and the weight of

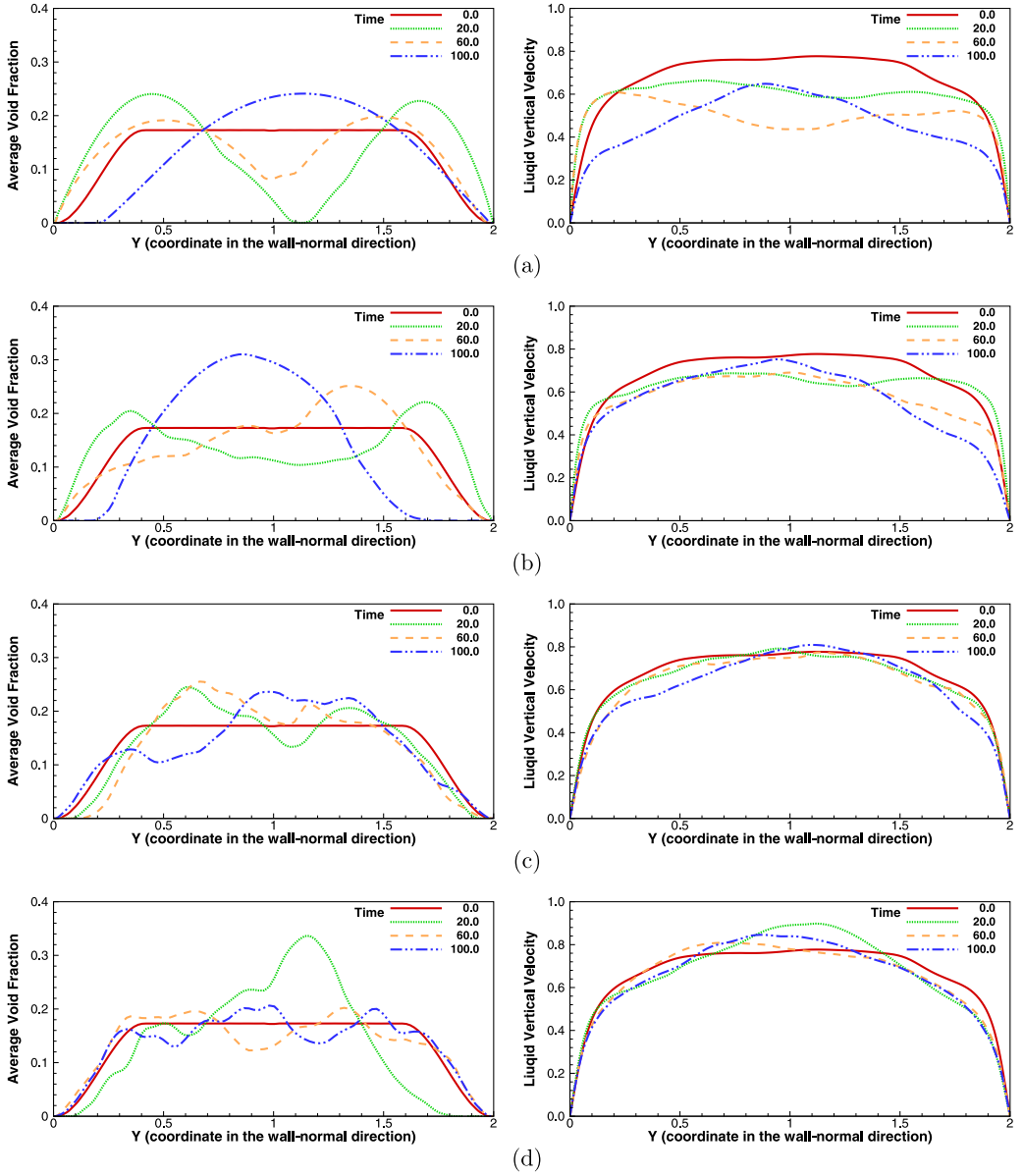

FIG. 7. The void fraction (left) and the average liquid velocity (right) versus the wall-normal coordinate for all four cases. (a) case 1; (b) case 2; (c) case 3; (d) case 4.

the mixture. The total surface area is shown in Fig. 8(d), and here it is clear that for the high surface tension cases the area decreases as the bubbles merge, whereas for the lowest surface tension the breakup increases the surface area. The total surface area tells us only about the average size of the bubbles and in the bottom row we show the projected surface area (or components of the surface area tensor) in two directions, normalized by dividing the projected surface area by the total area, in an attempt to see if the shapes are different, independently of the size and number of bubbles. For spherical bubbles the normalized projected area is 0.5 in all directions [twice the area of a circle, since the bubble has two sides, divided by the surface area of a sphere, or $2(n\pi d^2/4)/(n\pi d^2)$].

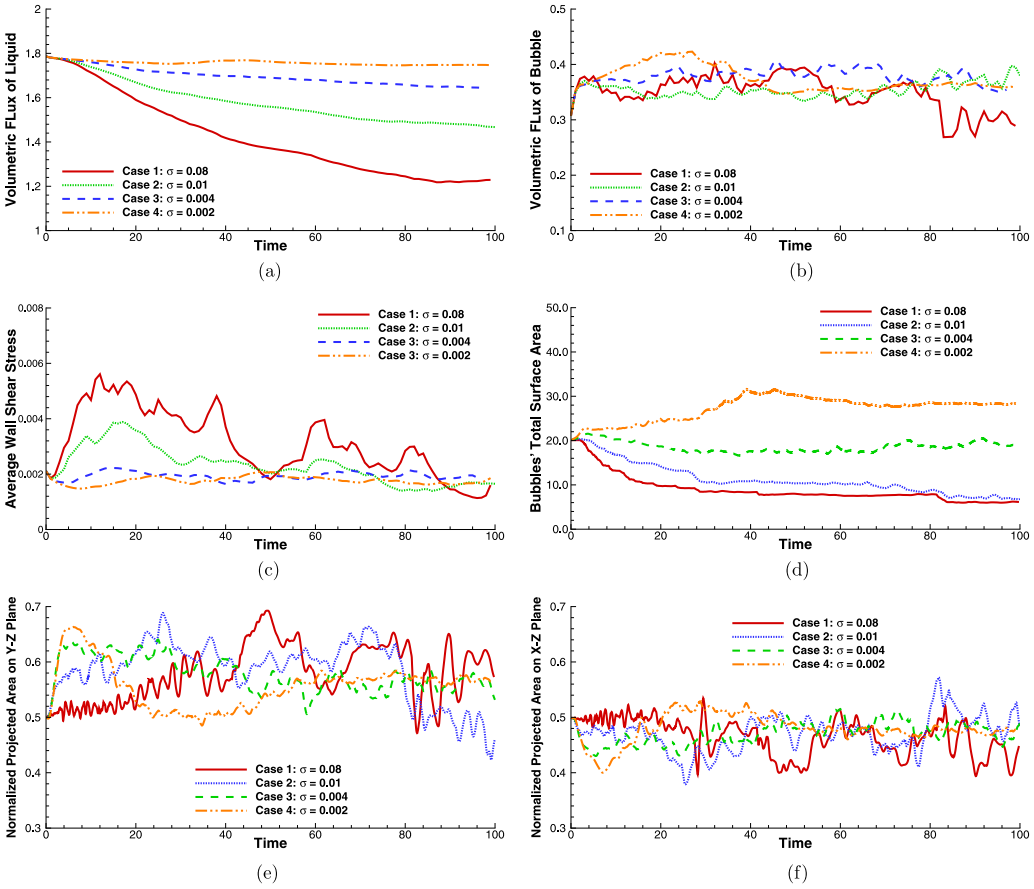

FIG. 8. Various averaged quantities for the different cases versus time. (a) The volumetric flow of the heavy fluid; (b) the volumetric flow of the light fluid; (c) the average wall shear stress; (d) the total interface area; (e) normalized projections of the surface area in the y-z plane; (f) normalized projections of the surface area in the x-z plane.

Figure 8(e) shows the projection in the streamwise direction, onto the y-z plane, and Fig. 8(f) shows the projection in the wall-normal direction, onto the x-z plane. The projected areas start out equal since the bubbles are initially spherical, but as they evolve the projected areas diverge as the shape changes. The differences in the y-z and the x-z projections are indicative of the deformation of the bubbles, and it is clear, for example, that the highest surface tension bubble is ellipsoidal near the end, whereas the lowest surface tension bubbles have projections that are comparable in both directions, although they are obviously very deformed after the initial coalescence. The x-y projection is not included since it is similar to the x-z projection.

To attempt to understand better the change in scale of the phase distribution, we have computed the size and number of equivalent bubbles from the volume and surface area for each case versus time. If we assume that the light fluid consists of n spherical bubbles with diameter d, then the total volume is $V = n(\pi/6)d^3$ and the total surface area is $A = n\pi d^2$. Given the volume and the surface area we can solve for the diameter and number of the bubbles: $d = 6V/A$ and $n = (\pi/36)(A/V)^2$. The bubble diameter is the well-known Sauter mean diameter often used in sprays. In Fig. 9 we plot the effective diameter (Sauter mean diameter) and equivalent number of bubbles versus time. For the higher surface tension cases the number of bubbles decreases, and the equivalent diameter continues to grow, approaching the values we would expect for one bubble (equal to 1.368, for the spherical

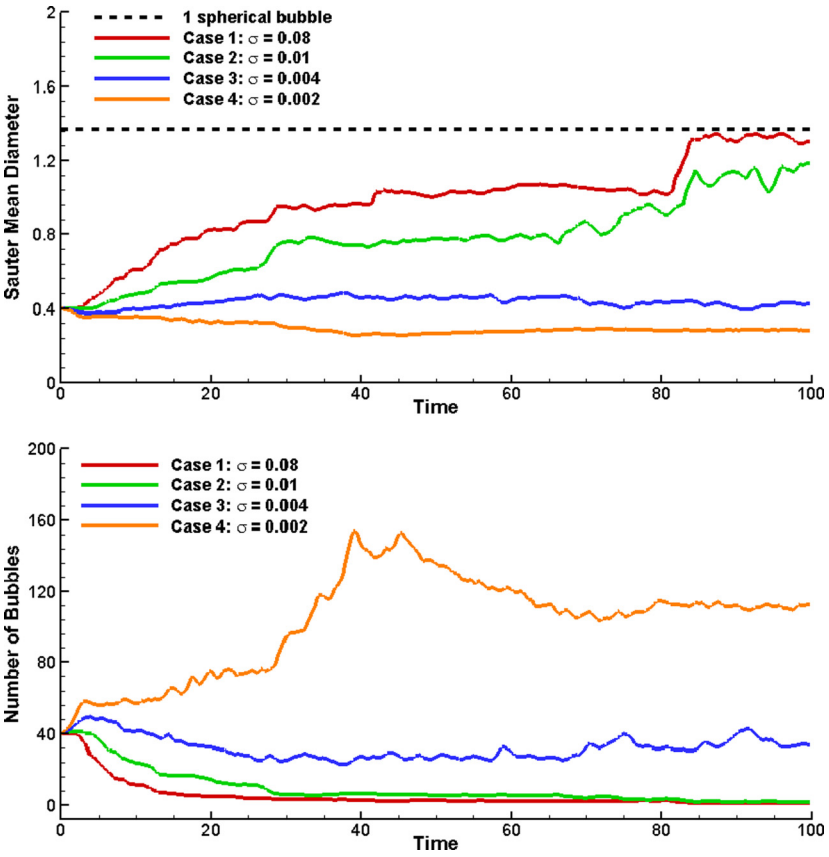

FIG. 9. The Sauter mean diameter (top) and the equivalent number of bubbles (bottom) versus time for all four cases.

bubble). The number of bubbles in the lower surface tension cases, on the other hand, approaches a finite value. For the lowest surface tension this value is significantly higher than the initial number of bubbles and the diameter is lower, but for the case with the second lowest value the number and size is comparable to the initial conditions.

In addition to the time evolution of the overall averaged quantities, we have also monitored the shape of the various profiles averaged over planes parallel to the walls. In Fig. 10 we examine a few of those at later stages where the evolution is approximately at steady state. Each profile has been obtained by averaging over 16 times between 85 and 100. The top row shows the average velocity of the heavy fluid in Fig. 10(a) and the void fraction in Fig. 10(b). The average velocity for the highest surface tension case is obviously smallest, and maximum at the center where the bubble is, and the velocities of the two lowest surface tension case are comparable. Similarly, the void fraction profiles for the high surface tension cases are similar and peaked in the center, but for the lower surface tension cases they are more uniform. The Reynolds stresses, in Fig. 10(c), are zero at the wall, become negative on the left-hand side, and then increase across the channel, becoming positive around the middle of the channel until dropping to zero at the right wall. This is comparable to what we expect in a single-phase flow. The stresses are lowest for the large bubble in the high surface tension cases and similar for the two lowest surface tension cases. The second highest surface tension case does, however, show largest variations, possibly due to the strong wake behind the bullet like shaped bubble (see Fig. 6). The area concentration, in Fig. 10(d), is found by assigning the area of each surface element to the nearest grid points, in the same way that surface tension and the density

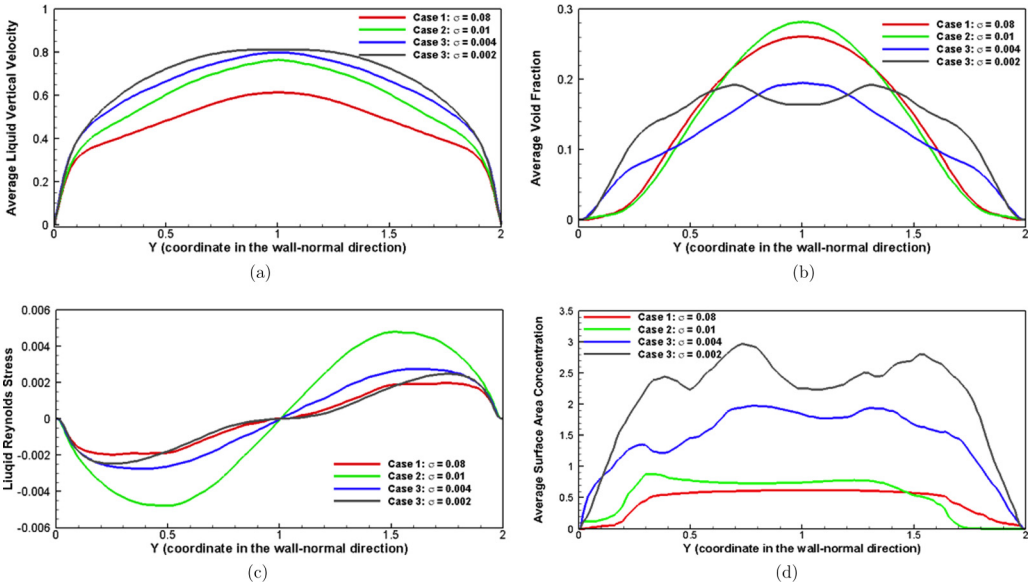

FIG. 10. The various averaged quantities versus the wall-normal coordinate, for all four cases after the flow has reached an approximate steady state. (a) The average velocity of the heavy fluid; (b) the void fraction of the light fluid; (c) the Reynolds stresses; (d) the area concentration.

gradient is treated in the front tracking code, and integrating over planes parallel to the walls. We have also differentiated the discontinuous density to get a delta function at the interface and found the area by integrating the delta function on the fluid grid. The results are nearly the same, but the latter approach gives a slightly lower value since gradients of the density cancel for interfaces close to each other. The average surface area concentration is lowest for the highest surface tension case, as expected, and highest for the lowest surface tension case where the bubble size is smallest.

To examine the phase distribution in more detail, we have computed a few statistical correlation functions. Statistical correlation functions are widely used to quantify the structure of heterogeneous material, as discussed by Ref. [41]. The two-point pair-probability function has, in particular, often been used to characterize disperse flows (see Ref. [42], for example) and in Ref. [34] it was used to analyze DNS data for bubbly flows, showing that while nearly spherical bubbles tend to line up horizontally, more deformable bubbles line up vertically. For disperse flows we usually need only the location of the centroid of each bubble, but here we work with the full field.

We define an indicator function χ such that $\chi = 1$ in one fluid and $\chi = 0$ in the other fluid. The two-point correlation function for the fluid where $\chi = 1$ is then defined as

$$S_2(r) = \langle \chi(\mathbf{x})\chi(\mathbf{x}+\mathbf{r})\rangle, \tag{2}$$

where the brackets $\langle\ \rangle$ denote the appropriate average. Obviously $\chi(\mathbf{x})\chi(\mathbf{x}+\mathbf{r}) = 1$ if $\mathbf{x}$ and $\mathbf{x}+\mathbf{r}$ are both in the fluid with $\chi = 1$, but zero if one or both points are in the fluid where $\chi = 0$. In the most general case the average is an ensemble average over many realization, but for systems that are homogeneous in one or more direction we can use a spatial average in the homogeneous directions and a temporal average if the system is at a statistically steady state. For our channel we focus on the approximately steady state and average over planes parallel to the walls and over time.

In material modeling the reconstructuring of heterogeneous materials from limited statistical information allows researchers to produce complete samples that then can be subjected to detailed analysis, such as determining the various macroscopic properties. Low-order probability functions are easiest both to measure and understand, but in Ref. [43] it was shown that the use of the two-point probability function only generally did not contain enough information to reconstruct the medium.

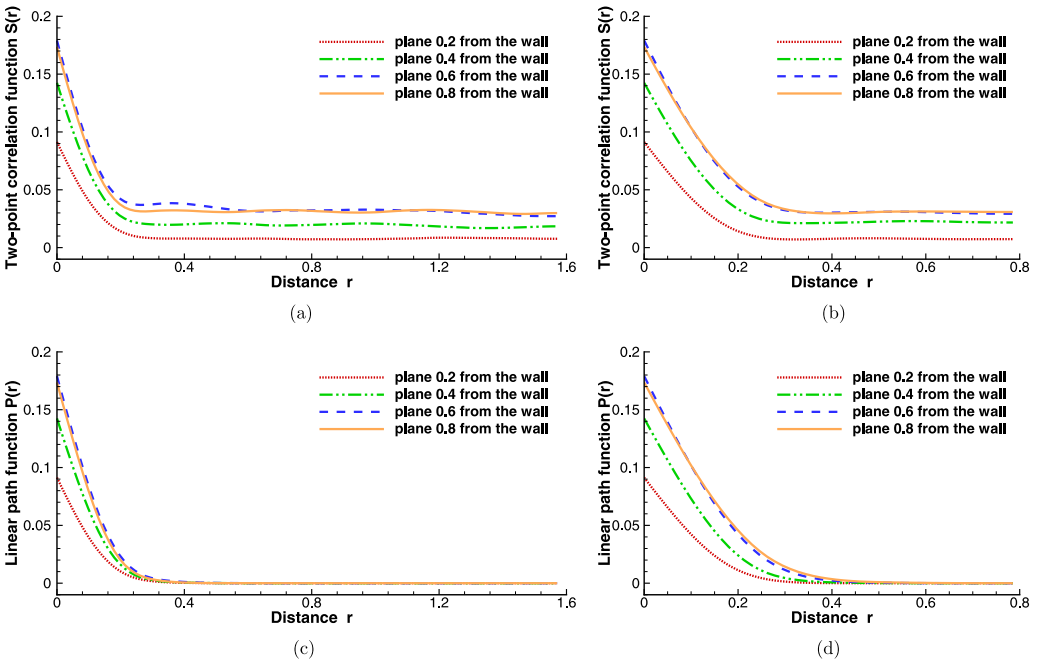

FIG. 11. Correlation functions for case 4 in three planes parallel to the walls after the flow has reached an approximately steady state. (a) Streamwise two-point correlation function; (b) spanwise two-point correlation function; (c) streamwise linear path correlation function; (d) spanwise linear path correlation function.

However, the linear path function L_2, defined as the probability of a line segment of a given length lying entirely within one phase, gave better results, and using both the two-point probability function and the linear path function gave better results.

We have examined both the two-point probability function and the linear path function, after the flow reaches an approximate steady state (time between 85 and 100) for all four cases and for both the heavy and the light fluid. The two-point correlation function is found by averaging over all the grid points in each plane, multiplying the indicator function at each point by the indication function at grid points a given distance away. The linear path function is found by averaging over all the grid points in each plane, multiplying the indicator function there by the indicator function at every point on a straight line between the point being considered and points a given distance away. The results are computed for four planes parallel to the walls, at 16 time intervals, and averaged over the left and right sides of the domain.

Figure 11 shows the correlation functions for the light fluid for case 4. The streamwise two-point correlation function is plotted in Fig. 11(a), the spanwise two-point correlation function in Fig. 11(b), the streamwise linear path correlation function in Fig. 11(c), and the spanwise linear path correlation function in Fig. 11(d). Since the domain is periodic in the streamwise and spanwise direction, we plot the functions only for half the streamwise and spanwise size of the domain. For zero distance between the points, $\mathbf{r} = 0$, the pointwise value is simply the probability of a point being in the light fluid, or its volume fraction, and both the two-point and the linear path correlation functions yield the average volume fraction at the corresponding distance to the wall, as expected. The correlations then decay as the correlation length increases. At large distance the two-point correlation function approaches the joint probability of finding two independent points both in the light fluid, or the volume fraction squared, if the indicator field is uncorrelated at large distances, and we see this for the two-point correlation function. For the linear path correlation functions we expect it to always cross the interface between the different fluids for long enough distances and thus approach zero, as

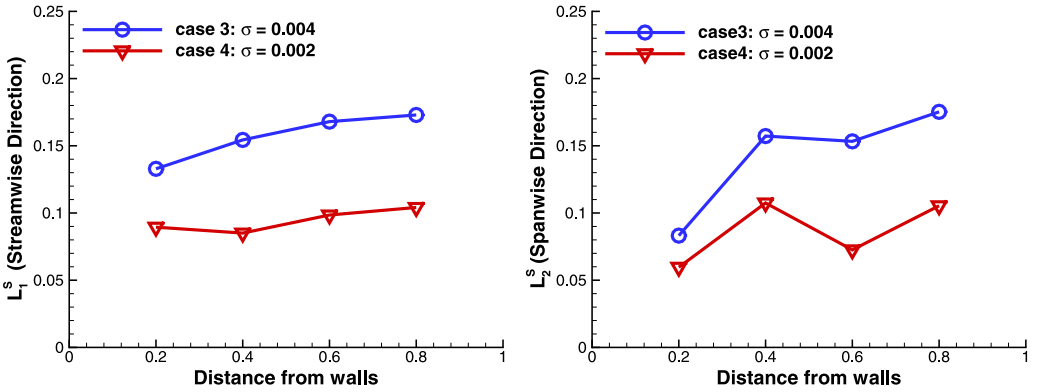

FIG. 12. Integral scales for the distribution of the light fluid versus the wall-normal coordinate for cases 3 and 4. ℓ_1^S in the streamwise direction on the left and ℓ_2^S in the spanwise direction on the right.

it does. See Ref. [41] for a discussion of the general behavior of the various correlation functions. In the middle of the channel, where the volume fraction is nearly constant, the correlations for the planes at 0.6 and 0.8 from the wall are nearly identical. Closest to the wall the spanwise and the streamwise correlations are essentially identical, but in the middle of the channel the spanwise correlations decay slightly more rapidly than the spanwise ones for both the two-point and linear path correlation. Notice that the distance where the streamwise correlations become a constant corresponds roughly to the Sauter mean diameter for this case (see Fig. 9).

We have also examined the correlation functions for the other cases, as well as for the distribution of the heavy fluid. The results show that the correlation functions for the light fluid for case 3 is similar to case 4 but converge more slowly, and the spanwise correlations have barely reached their expected asymptotic values for a distance equal to half the channel width. For cases 1 and 2, where the light fluid coalesces into one big bubble, the streamwise two-point correlation and the linear path functions are identical and converge to zero, as we expect for fluid contained in one large bubble, and although the spanwise correlations have decreased, they have not converged for a distance equal to half the channel width. For the heavy fluid the two-point correlation function in the streamwise direction for cases 1 and 2 converges to the expected asymptotic value (volume fraction squared) at a rate that is much slower than for cases 3 and 4, but the linear path function converges much more slowly and has not reached its asymptotic value for a separation distance equal to half the channel for any of the cases.

To compare the correlation functions in quantitative ways we define two length scales by the integral of the scaled two-point correlation function and the square root of the first moment of the scaled two-point correlation function

$$\ell_1^S = \frac{1}{Q(0)} \int_0^{L_x/2} Q(r)\, dr, \quad \ell_2^S = \sqrt{\frac{1}{Q(0)} \int_0^{L_x/2} r\ Q(r)\, dr}, \tag{3}$$

where $Q(r) = S_2(r) - \alpha^2$ and α is the local void fraction. In Fig. 12 we plot ℓ_1^S (on the left) and ℓ_2^S (on the right) for the streamwise correlation for the light fluid versus the wall-normal coordinate for cases 3 and 4. For cases 1 and 2 the streamwise two-point correlation function converges to zero, rather than to the square of the void fraction expected for phase distribution that is uncorrelated at large separation distances. The integral length scales behave similarly for both cases, increasing slightly with the distance from the wall. The integral scales for the spanwise distribution show a similar behavior. While similar integral scales can be defined for the linear path function [taking $Q(r) = L_2$ in Eq. (3)], those have reached zero only at the maximum separation for the light fluid for cases 3 and 4, so a similar comparison would be less conclusive.

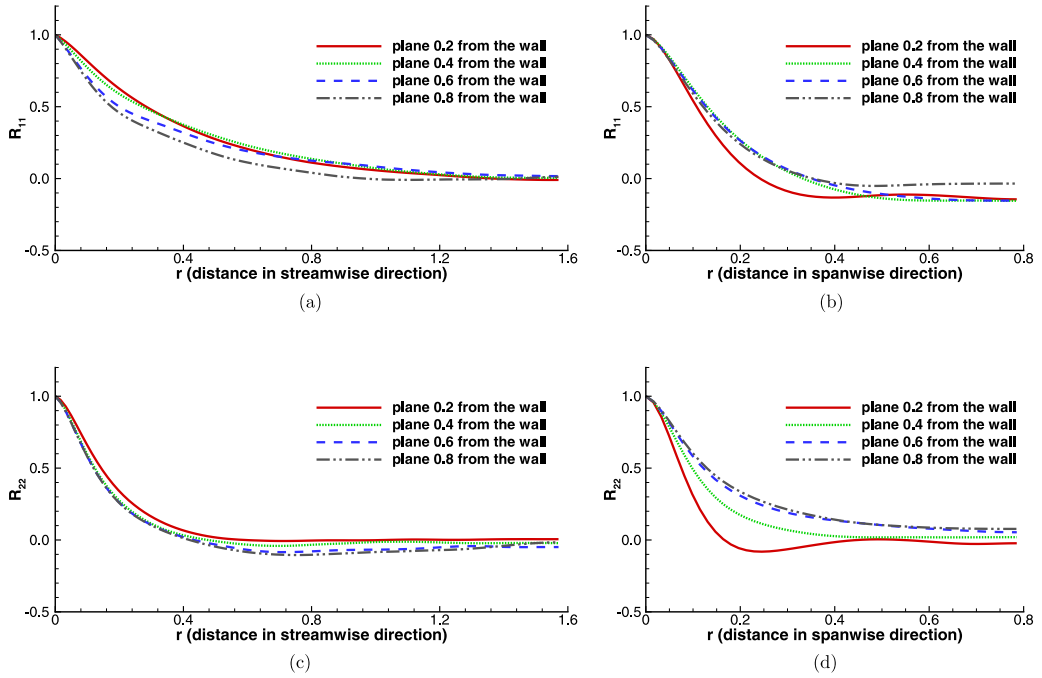

FIG. 13. Two-point correlation functions for the velocity fluctuations for case 4. (a) Correlation of streamwise velocities in streamwise direction; (b) correlation of streamwise velocities in spanwise direction; (c) correlation of spanwise velocities in streamwise direction; (d) correlation of spanwise velocities in spanwise direction.

We have examined the velocity fluctuations in the same way. The conditional correlation function for the velocity fluctuations, that is, the correlation between the fluctuation velocity at two different points in the same fluid, is given by

$$R_{ij} = \frac{\langle \chi(\mathbf{x}) u_i'(\mathbf{x}) \chi(\mathbf{x}+\mathbf{r}) u_j'(\mathbf{x}+\mathbf{r}) \rangle}{\langle \chi(\mathbf{x}) u_i'(\mathbf{x}) u_j'(\mathbf{x}) \rangle} \tag{4}$$

and is found in planes parallel to the walls, in the same way as the correlation function for the phase distribution. Here i, $j = 1$, 2, or 3, for the streamwise, wall-normal, and spanwise direction, respectively. It is divided by the single-point correlation function to obtain a value of unity for $\mathbf{r} = 0$. In Fig. 13 we plot the correlation function for the velocity fluctuations in the heavy fluid, for four planes parallel to the wall, for case 4. The top row shows correlation for the streamwise velocity fluctuations, and the bottom row shows the wall-normal velocity fluctuations. The correlations in the streamwise direction are shown on the left and in the spanwise direction on the right. In all cases the correlations decay to zero, but the correlation of the streamwise velocity in the streamwise direction decays more slowly than the wall-normal component as well as the correlations for both components in the spanwide direction. For each frame the decay is nearly the same for all distances to the wall, except for the spanwise correlation closest to the wall. We have computed various other velocity fluctuation correlations for other velocity components and the other cases. The results for case 3 are similar, but for cases 1 and 2 we see slower decay, particularly for the streamwise fluctuations.

We can compute integral length scales from the conditional correlation function for the velocity fluctuations in the same way as we did for the phase distribution, but here we examine only ℓ_1^R

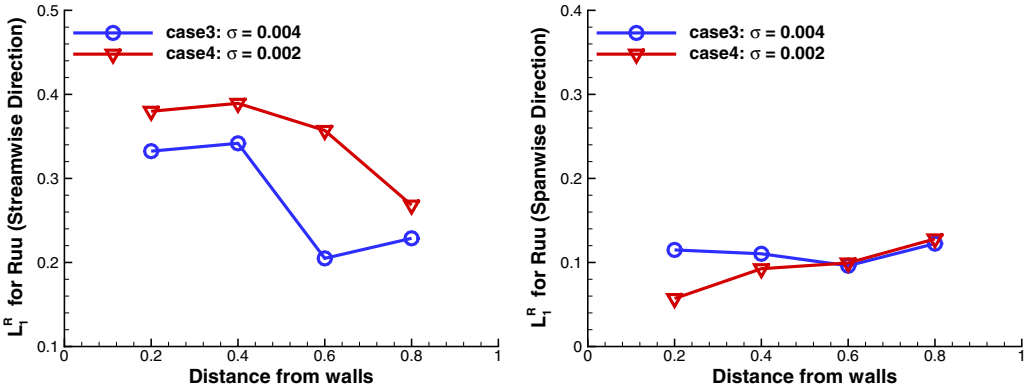

FIG. 14. Integral scale for the streamwise velocity fluctuations. Streamwise direction on the left and spanwise direction on the right.

defined by

$$\ell_1^R = \int_0^\infty R(r)\, dr. \tag{5}$$

A meaningful comparison requires a converged correlation function, so in Fig. 14 we examine only the integral scales for cases 3 and 4, and only for the streamwise fluctuations. The integral scale is plotted versus the wall-normal coordinate for the streamwise fluctuations in the frame on the left and for the spanwise direction on the right. The integral scale in the streamwise direction is larger than in the spanwise direction, but both remain nearly constant across the channel.

We note that we have simulated only one domain size. For the highest surface tension, where the final result is one single bubble, it is obvious that the results will be different in longer domains. For the smallest surface tension cases we believe that the fact that the void fraction and the velocities are uncorrelated, as Figs. 11–14 show, suggests that we would get similar results in a longer domain.

V. CONCLUSIONS

We have examined the evolution of two fluids of different properties in a turbulent channel flow where the interface separating the light and the heavy fluid is allowed to undergo topology changes. The light fluid is initially contained in several distinct bubbles (or light drops) that then collide and coalesce. Four cases are examined. In two case the surface tension is relatively large, and the bubbles continually merge until all the light fluid is contained in one large bubble. In the other cases the bubbles coalesce and then break up again.

The focus here has been on quantifying the evolutions and, in particular, characterize the distribution of the different fluids and interface topology. Finding a way to bring out the difference in the distribution of bubble sizes as the surface tension changes, however, remains to be done. A visual observation, for example, suggests that the long time bubble distribution will generally consist of several large and many small bubbles and that the size difference decreases as surface tension is reduced and increases as surface tension is increased, with the limits being one large bubble for high surface tension and many bubbles of the same size for low surface tension.

We note that this study, where we attempt to characterize a complex multiphase flows undergoing rapid topology changes, is a challenging topic that brings together a number of fields. The ultimate goal is to be able to develop the insight and the data needed to improve average two-fluid and LES-like models, but for the characterization of the topology we need input from studies of random heterogeneous materials [41], as well as the dynamic evolution of interfaces undergoing mixing, such as those studied in rheology and turbulent combustion [44–46]. Exactly how progress made

in these diverse field can be harnessed to help us understand the evolution is, however, an ongoing study. We note, in particular, that the goals here are a little different than for studies of heterogeneous solid materials where low-order correlation functions can sometimes be found experimentally and several authors have used those to construct representative materials that can then be used to find the various material properties. Here we are not attempting to do that, since we already have a complete description of the flow and the interface, but simply use the correlation functions to diagnose the flow and the structure of the phase distribution.

We have focused here on the effect of surface tension, since understanding the evolution of the topology is likely to affect modeling of the flow. From a practical point of view, however, it is the change of the flow structure as the void fraction changes that is critical. We expect to examine that aspect in future studies.

ACKNOWLEDGMENT

This research was supported by the Consortium for Advanced Simulation of Light Water Reactors, an Energy Innovation Hub for Modeling and Simulation of Nuclear Reactors under US Department of Energy Contract No. DE-AC05-00OR22725.

[1] W. Dijkhuizen, I. Roghair, M. Van Sint Annaland, and J. Kuipers, DNS of gas bubbles behavior using an improved 3d front tracking model–drag force on isolated bubbles and comparison with experiments, Chem. Eng. Sci. **65**, 1415 (2010).

[2] W. Dijkhuizen, I. Roghair, M. Van Sint Annaland, and J. Kuipers, DNS of gas bubbles behavior using an improved 3d front tracking model—Model development, Chem. Eng. Sci. **65**, 1427 (2010).

[3] M. van Sint Annaland, W. Dijkhuizen, N. G. Deen, and J. A. M. Kuipers, Numerical simulation of gas bubbles behavior using a 3D front tracking method, AIChE J. **52**, 99 (2006).

[4] M. K. Tripathi, K. C. Sahu, and R. Govindarajan, Dynamics of an initially spherical bubble rising in quiescent liquid, Nat. Commun. **6**, 6268 (2015).

[5] D. M. Sharaf, A. R. Premlata, M. K. Tripathi, B. Karri, and K. C. Sahu, Shapes and paths of an air bubble rising in quiescent liquids, Phys. Fluids **26**, 122104 (2017).

[6] M. K. Tripathi, A. R. Premlata, K. C. Sahu, and R. Govindarajan, Two initially spherical bubbles rising in quiescent liquid, Phys. Rev. Fluids **2**, 073601 (2017).

[7] B. Bunner and G. Tryggvason, Effect of bubble deformation on the stability and properties of bubbly flows, J. Fluid Mech. **495**, 77 (2003).

[8] A. Esmaeeli and G. Tryggvason, A DNS study of the buoyant rise of bubbles at O(100) Reynolds numbers, Phys. Fluids **17**, 093303 (2005).

[9] J. Lu and G. Tryggvason, Effect of bubble size in turbulent bubbly downflow in a vertical channel, Chem. Eng. Sci. **62**, 3008 (2007).

[10] J. Lu and G. Tryggvason, Dynamics of nearly spherical bubbles in a turbulent channel upflow, J. Fluid Mech. **732**, 166 (2013).

[11] I. A. Bolotnov, R. T. Lahey, D. A. Drew, and K. E. Jansen, Turbulent cascade modeling of single and bubbly two-phase turbulent flows, Int. J. Multiphase Flow **34**, 1142 (2008).

[12] I. A. Bolotnov, K. E. Jansen, D. A. Drew, A. A. Oberai, R. T. Lahey, and M. Z. Podowski, Detached direct numerical simulations of turbulent two-phase bubbly channel flow, Int. J. Multiphase Flow **37**, 647 (2011).

[13] I. A. Bolotnov, Influence of bubbles on the turbulence anisotropy, J. Fluids Eng. **135**, 051301 (2013).

[14] J. M. Rodriguez, O. Sahni, R. T. Lahey Jr., and K. E. Jansen, A parallel adaptive mesh method for the numerical simulation of multiphase flows, Comput. Fluids **87**, 115 (2013).

[15] J. O. McCaslin and O. Desjardins, Numerical investigation of gravitational effects in horizontal annular liquid—Gas flow, Int. J. Multiphase Flow **67**, 88 (2014).

[16] J. Shinjo and A. Umemura, Simulation of liquid jet primary breakup: Dynamics of ligament and droplet formation, Int. J. Multiphase Flow **36**, 513 (2010).
[17] G. Tomar, D. Fuster, S. Zaleski, and S. Popinet, Multiscale simulations of primary atomization, Comput. Fluids **39**, 1864 (2010).
[18] M. Herrmann, Detailed numerical simulations of the primary atomization of a turbulent liquid jet in crossflow, J. Eng. Gas Turbines Power **132**, 061506 (2010).
[19] Y. Taitel, D. Bornea, and A. E. Dukler, Modeling flow pattern transitions for steady upward gas-liquid flow in vertical tubes, AIChE J. **26**, 345 (1980).
[20] N. K. Tutu, Pressure fluctuations and flow pattern recognition in vertical two-phase gas-liquid flows, Int. J. Multiphase Flow **8**, 443 (1982).
[21] Z. Bilicki and J. Kestin, Transition criteria for two-phase flow patterns in vertical upward flow, Int. J. Multiphase Flow **13**, 283 (1987).
[22] T. Yoshinaga and Y. Sato, Performance of an air-lift pump for conveying coarse particles, Int. J. Multiphase Flow **22**, 223 (1996).
[23] R. Rozenblit, M. Gurevich, Y. Lengel, and G. Hetsroni, Flow patterns and heat transfer in vertical upward air-water flow with surfactant, Int. J. Multiphase Flow **32**, 889 (2006).
[24] A. Manera, H.-M. Prasser, D. Lucas, and T. H. J. J. van der Hagen, Three-dimensional flow pattern visualization and bubble size distributions in stationary and transient upward flashing flow, Int. J. Multiphase Flow **32**, 996 (2006).
[25] G. F. Hewitt and D. N. Roberts, Studies of two-phase flow patterns by simultaneous X-rays and flash photography, Technical Report M-2159, Atomic Energy Research Establishment Harwell, England (1969).
[26] G. B. Wallis, *One-Dimensional Two-Phase Flow* (McGraw-Hill, New York, 1969).
[27] V. C. Samaras and D. P. Margaris, Two-phase flow regime maps for air-lift pump vertical upward gas-liquid flow, Int. J. Multiphase Flow **31**, 757 (2005).
[28] S. Guet and G. Ooms, Fluid mechanical aspects of the gas-lift technique, Annu. Rev. Fluid Mech. **38**, 225 (2006).
[29] R. D. Falgout, J. E. Jones, and U. M. Yang, The design and implementation of HYPRE, a library of parallel high performance preconditioners, in *Numerical Solution of Partial Differential Equations on Parallel Computers*, Vol. 51, edited by A. M. Bruaset and A. Tveito (Springer-Verlag, New York, 2006), pp. 267–294.
[30] G. Tryggvason, R. Scardovelli, and S. Zaleski, *Direct Numerical Simulations of Gas-Liquid Multiphase Flows* (Cambridge University Press, Cambridge, 2011).
[31] C. S. Peskin, Numerical analysis of blood flow in the heart, J. Comput. Phys. **25**, 220 (1977).
[32] S. O. Unverdi and G. Tryggvason, A front-tracking method for viscous, incompressible, multi-fluid flows, J. Comput. Phys. **100**, 25 (1992).
[33] G. Tryggvason, B. Bunner, A. Esmaeeli, D. Juric, N. Al-Rawhai, W. Tauber, J. Han, S. Nas, and Y.-J. Jan, A front tracking method for the computations of multiphase flow, J. Comput. Phys. **169**, 708 (2001).
[34] B. Bunner and G. Tryggvason, Dynamics of homogeneous bubbly flows Part 1. Rise velocity and microstructure of the bubbles, J. Fluid Mech. **466**, 17 (2002).
[35] S. Biswas, A. Esmaeeli, and G. Tryggvason, Comparison of results from DNS of bubbly flows with a two-fluid model for two-dimensional laminar flows, Int. J. Multiphase Flow **31**, 1036 (2005).
[36] Y. Hao and A. Prosperetti, A numerical method for three-dimensional gas–liquid flow computations, J. Comput. Phys. **196**, 126 (2004).
[37] J. Hua and J. Lou, Numerical simulation of bubble rising in viscous liquid, J. Comput. Phys. **222**, 769 (2007).
[38] M. Muradoglu and A. D. Kayaalp, An auxiliary grid method for computations of multiphase flows in complex geometries, J. Comput. Phys. **214**, 858 (2006).
[39] J. F. Gibson, Channelflow: A spectral Navier-Stokes simulator in C++, Technical Report, University of New Hampshire (2014), `Channelflow.org`.
[40] J. F. Gibson, J. Halcrow, and P. Cvitanović, Visualizing the geometry of state space in plane Couette flow, J. Fluid Mech. **611**, 107 (2008).
[41] S. Torquato, Statistical description of microstructures, Annu. Rev. Mater. Res. **32**, 77 (2002).

[42] A. J. C. Ladd, Dynamical simulations of sedimenting spheres, Phys. Fluids A **5**, 299 (1993).
[43] C. L. Y. Yeong and S. Torquato, Reconstructing random media, Phys. Rev. E **57**, 495 (1998).
[44] E. D. Wetzel and C. L. Tucker III, Area tensors for modeling microstructure during laminar liquid-liquid mixing, Int. J. Multiphase Flow **25**, 35 (1999).
[45] D. Lhuillier, Dynamics of interfaces and rheology of immiscible liquid-liquid mixtures, C. R. Mecanique **331**, 113 (2003).
[46] C. Morel, On the surface equations in two-phase flows and reacting single-phase flows, Int. J. Multiphase Flow **33**, 1045 (2007).